Discontinuous character of the ultrafast exciton Mott transition in monolayer WS_2

Subhadra Mohapatra [1], Samuel Palato [1], Nicholas Olsen [2], Julia Stähler [1,3] and Lukas Gierster [1,*]

[1] *Humboldt-Universität zu Berlin, Institut für Chemie, Berlin, Germany*

[2] *Department of Chemistry, Columbia University, New York, USA*

[3] *Fritz-Haber-Institut der Max-Planck-Gesellschaft, Abt. Physikalische Chemie, Berlin, Germany*

(Received 3 March 2026; revised 7 August 2026; accepted 14 October 2026; published 3 November 2026)

There are conflicting predictions and reports on the character of the exciton Mott transition (EMT) in monolayer transition metal dichalcogenides. It could be either a discontinuous or a continuous transition from the excitonic to the plasma phase, with important implications for devices such as photoswitches. To resolve the nature of the transition in monolayer WS_2, we study its ultrafast optical response upon resonant photoexcitation of the A exciton across a broad range of photoexcitation densities. In agreement with previously reported measurements, we observe that the A exciton quenches gradually with increasing excitation density. However, a detailed lineshape analysis unveils an abrupt red shift in the transient peak positions of the A and B exciton resonances above an excitation density threshold. This is attributed to band gap renormalization arising from the formation of a free charge carrier plasma, i.e., the EMT. The plasma phase decays with a time constant of 0.65 ps into the excitonic state. The abrupt appearance of the plasma phase at the threshold density suggests that the EMT is a discontinuous and not a continuous transition. This work demonstrates how transient optical spectroscopy combined with simultaneous lineshape analysis of two excitonic resonances can be used to investigate the EMT in 2D materials.

DOI: 10.1103/hh6p-dpf7

I. INTRODUCTION

Strong light–matter interaction and large exciton binding energies make atomically thin TMDCs promising systems for fundamental studies and applications [1–3]. At low charge carrier densities, excitons govern the optical and electronic properties, whereas at a critical (Mott) density, enhanced screening weakens the Coulomb attraction between electrons and holes and leads to dissociation of the exciton gas into a metal-like electron–hole plasma—the EMT. This transition has been intensely studied [4–14], both because device concepts such as excitonic optoelectronics, valleytronics, and nanolasers depend on the balance of free carriers and excitons [15], and because high densities enable exploration of many-body physics, including the electron–hole liquid with its exotic correlated properties [16,17]. The large binding energies in TMDCs yield strong excitonic signatures even at room temperature, suggesting that optical spectroscopy should readily probe the EMT. Yet for monolayers—with direct band gaps and the highest binding energies—it remains unclear whether the EMT evolves continuously with increasing excitation density, via coexistence of excitons and plasma, or discontinuously, as an abrupt or avalanche-like transition [18]. Resolving this is crucial for device design and for understanding photoexcited TMDC monolayers at high densities. Moreover, an ultrafast, discontinuous EMT could enable novel TMDC-based photoswitches and potentially access exotic quantum phases.

Theoretically, both continuous and discontinuous EMTs are possible. Material-realistic many-body calculations using GW-DFT and Bethe–Salpeter methods predict that a small exciton fraction (1%) dissociates below the Mott density, followed by an abrupt jump to full ionization [13]. Such an abrupt jump is calculated for WS_2, WSe_2, MoS_2, and $MoSe_2$ TMDC monolayers [13] and suggests a discontinuous character of the EMT. In contrast, a more conceptual study using a half-filled Hubbard model mapped to the exciton problem argues that the EMT character depends on the exciton binding energy [14], which varies with TMDC composition.

Experimentally, EMT studies have focused mainly on bilayers [4–8], heterostructures [4,9], and bulk TMDCs [19,20]. For monolayer TMDCs, however, only limited and conflicting observations exist. In MoS_2, continuous wave excitation reveals an abrupt switch from narrow exciton emission to broad electron–hole plasma emission at the Mott density [10], later linked to an electron–hole liquid [16]. By contrast, WSe_2 and $MoSe_2$ monolayers show a continuous EMT, evidenced by continuously broadened time-integrated photoluminescence under ultrafast excitation [11]. Ultrafast time-resolved EMT measurements have so far been reported only for WS_2 [12], where pump–probe spectroscopy shows a gradual quenching of the A exciton resonance (AX) and the simultaneous emergence of stimulated emission below the optical gap because of plasma-induced band-gap renormalization (BGR)

*Contact author: lukas.gierster@hu-berlin.de

Published by the American Physical Society under the terms of the Creative Commons Attribution 4.0 International license. Further distribution of this work must maintain attribution to the author(s) and the published article's title, journal citation, and DOI.

over a large (> 1 order of magnitude) pump laser fluence range [12]. The coexistence of exciton and plasma signals supports a continuous EMT in WS_2 [14]. These differing behaviors across monolayer compositions may reflect the Mott–Hubbard model [14], but they contrast with *ab initio* predictions of an abrupt EMT [13].

The above observations do not permit firm conclusions. On the one hand, the time-resolved measurements in WS_2 show that the plasma decays on a few-picosecond timescale, while the overall photoexcited state relaxes much more slowly [12]. Thus, the continuous EMT inferred for WSe_2 and $MoSe_2$ from time-integrated photoluminescence must be interpreted cautiously: if the plasma rapidly relaxes into excitons, their luminescence will mix with plasma emission even if the initial transition is abrupt. On the other hand, in the time-resolved measurements on WS_2, the mere persistence of an excitonic resonance does not guarantee stable excitons, because collective Coulomb screening develops on ultrafast timescales comparable to the inverse plasma frequency [21]. Transient excitons can even appear at metal surfaces [22,23]. In bulk WSe_2, above the EMT, time-resolved x-ray photoelectron spectroscopy reports exciton dissociation within about 100 fs [19]. Therefore, in TMDCs probed with femtosecond pulses, an exciton resonance may still appear—even in a pure plasma phase—albeit broadened, shifted, or weakened by photoexcited carriers.

Fortunately, because of the clearly defined exciton resonances in TMDCs, these changes can be tracked in the ultrafast time domain using line shape analysis, as previously demonstrated for low excitation densities below the EMT [24–27]. Our previous work [24] showed that excitons, free charge carriers, and lattice heating can be disentangled in WS_2. For example, the presence of other excitons blue shifts the AX, while free charge carriers and lattice heating cause a red shift because of BGR. Applying such analysis to optical spectra across the EMT has so far been elusive. Furthermore, photoexciting one excitonic resonance can affect another excitonic resonance in the system. Transient absorption and 2D spectroscopy have shown that an A exciton population leads to an amplitude change of the second lowest energy B exciton resonance (BX) [28–31]. The shift dynamics have not been analyzed yet. Interestingly, *ab initio* calculations of optical pump-probe spectroscopy predict that the BX exhibits no shift upon photoexcitation of A excitons [32]. This could potentially make the BX shift an exclusive indicator for BGR and hence, the existence of free charge carriers when tuning the photoexcitation density across the EMT.

Here, we report a systematic study of the EMT in monolayer WS_2 through fluence-dependent ultrafast transient absorption (TA) spectroscopy combined with a detailed line-shape analysis of both the AX and the BX. Using photoexcitation resonant with the AX, we photoexcite the system across a broad range of excitation densities, in which the EMT is expected to occur, and track the temporal evolution of the optical response in the ultrafast time domain. In the low laser fluence regime, the AX position and width are determined by the pump-induced A exciton population and the heating of the lattice, as observed before [24]. We confirm the theoretical prediction [32] that the BX does not show an A exciton population-induced blue shift, but exclusively exhibits a red shift arising from the BGR induced by lattice heating and free charge carriers, which can be well separated because of their different decay times. As the excitation density increases, a gradual reduction of the oscillator strength of the AX is observed, in agreement with previous measurements [12]. This is attributed to population-induced bleaching. Well before the exciton resonance is completely bleached, the lineshape analysis of the differential spectra reveals an abrupt red shift of several tens of meV of the AX and the BX at a critical excitation density of $n_C = 29 \pm 2 \times 10^{12}$ cm^{-2} arising from BGR upon plasma formation. The plasma decays within 0.65 ps, leading to a recovery of the excitonic phase. The BX, being exclusively sensitive to BGR, can be used to track the plasma population across all excitation densities. Besides the abrupt jump at the critical density, a small amount of plasma is detected already at low excitation densities. The trend closely follows the prediction by *ab initio* many-body theory of Ref. [13]. The abrupt change of the excitonic resonances suggests that the EMT in WS_2 has a discontinuous character. This, combined with the previously reported discontinuous EMT in MoS_2, suggests that the different exciton binding energies in these systems do not play a significant role in the EMT character, contrary to theoretical predictions [14]. The excitonic resonances persist across the Mott transition, which is consistent with a finite dissociation time of photoexcited excitons to plasma. Our data show that the dissociation is completed within less than 200 fs. This work shows how optical spectroscopy can be used to investigate the Mott transition in 2D materials. In particular, we show that the inspection of several excitonic resonances at once can yield a comprehensive picture of the charge carrier dynamics across all excitation densities.

II. EXPERIMENTAL SECTION

To resolve the optical response of the WS_2 monolayer following resonant photoexcitation, we use TA spectroscopy, as sketched in Fig. 1(a). TA spectroscopy is a pump-probe technique, in which a first femtosecond laser pulse ("pump") photoexcites the system, and a second laser pulse ("probe") monitors the photoinduced changes of the absorption at variable delays. The monolayer sample is resonantly photoexcited at the A exciton, using a photon energy of 1.985 eV. A low fluence white-light continuum (WLC) probe pulse ranging from 1.8 to 4.5 eV is used to measure the absorption A of the sample across multiple excitonic transitions. The pump-induced change in the absorption is recorded as $\Delta A = A_{\text{pumped}} - A_{\text{unpumped}}$.

The experimental setup was described in detail previously in Refs. [33,34]. Briefly, the laser source for TA is a regeneratively amplified laser system (Astrella by Coherent), which outputs 30 fs laser pulses at a wavelength of 800 nm with a repetition rate of 5 kHz. The fundamental beam is split to produce separate pump and probe beam paths. In the pump beam path, the desired wavelength is generated using an optical parametric amplifier (Light Conversion TOPAS). In the probe beam path, the 800 nm light is frequency doubled and generates the WLC in a CaF_2 crystal. A delay stage (Physik Instrumente M-531.5IM) controls the time delay between the pump and probe pulses. The chirp of the white-light pulses

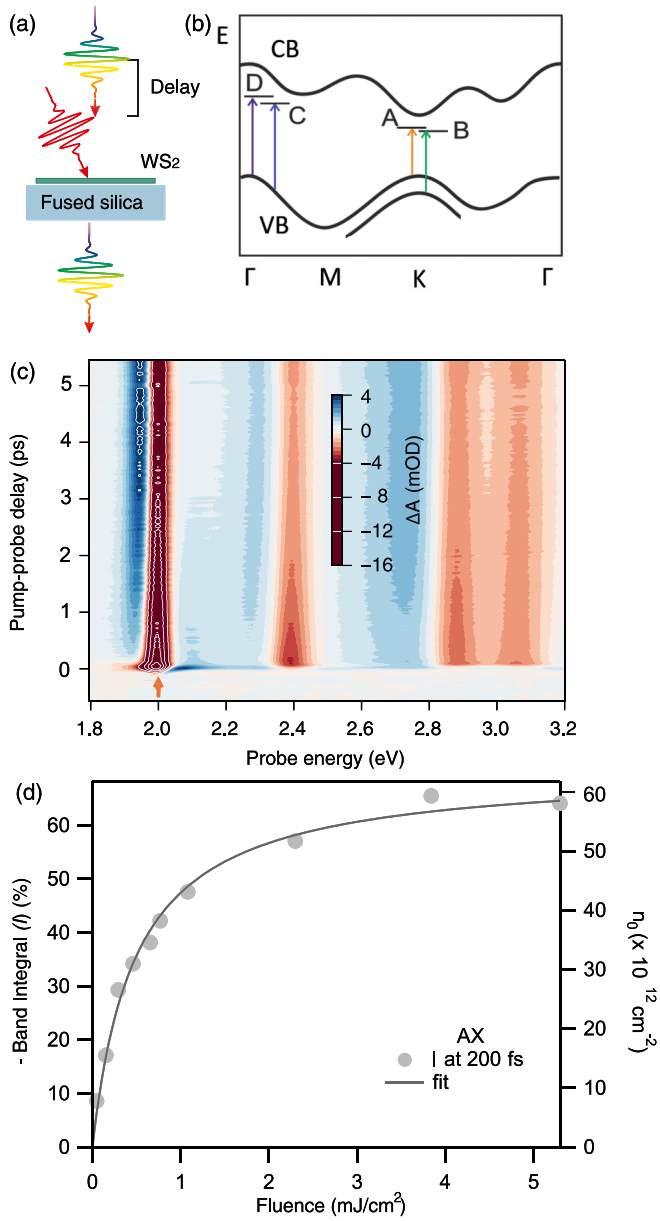


FIG. 1. (a) Sketch of TA applied to a WS_2 monolayer on a fused silica substrate. (b) Band diagram and excitonic resonances (AX, BX, CX, DX) in the monolayer inserted into the single-particle band structure as photoionization energy levels of the excitons. (c) Energy- and delay-dependent differential absorption spectra (color plot) of the monolayer photoexcited resonantly to the AX. (d) AX band integral at 200 fs relative to its steady-state value and fit with a saturable absorber model to determine the excitation density.

is corrected *a posteriori* and computationally with about 20 fs precision as described in Ref. [34]. The cross correlation of pump and probe laser pulses is on the order of 50 fs (FWHM).

To calculate the laser fluence, the spot sizes of pump- and probe laser pulses are characterized at the sample position with a CCD camera. Pump- and probe pulses have similar spot diameters of $d = 150$ μm (D4σ). The laser fluence is calculated using

$$F = \frac{2P}{AR} \tag{1}$$

with P the factor of 2 in Eq. (1), $A = \pi d^2/4$ and R the laser repetition rate. The factor of 2 accounts for the fluence at the center of a Gaussian beam profile (peak fluence). Since pump and probe spot sizes are approximately equal in our experimental configuration, the edge of the probe beam samples areas with lower excitation density as well. Therefore, our fluence calculation slightly overestimates the fluence. Under these nonideal conditions, our analysis probably overestimates the width changes and underestimates the peak shifts. However, as discussed in Sec. III B3, the quantitative results are in agreement with previous studies in the excitonic regime. Moreover, apparently the setting does not affect the spectra so much as to inhibit a sharp Mott transition as shown in Sec. III B4 and is therefore also not expected to severely affect the Mott density determined in this work.

The high-quality WS_2 monolayer on a fused silica substrate is prepared from its bulk counterpart using the gold-exfoliation technique, detailed in Refs. [35–37]. This method provides high-quality monolayers with fewer defects than commercially grown monolayers [15]. The flake size is several hundred micrometers. All measurements are performed at room temperature (22 °C).

III. RESULTS

The results section is structured as follows. First, we present a data set to define the observables and determine the excitation density. Then we present the kinetics below and across the Mott density.

A. Data and excitation density

An exemplary data set obtained for a single pump fluence at 150 μJ/cm^2 is shown in Fig. 1(c). The differential absorption (ΔA) is displayed as a function of pump-probe delay and probe energy. The false color plot shows weak positive (blue) and prominent negative (red) signals. They appear immediately at time zero (i.e., at the pump-probe overlap) and decrease partially within the first few picoseconds. Part of the signal extends beyond the shown delay window and survives up to the longest measured delay of 60 ps (not shown). The negative signals are centered around 1.99 eV, 2.38 eV, 2.88 eV, and 3.05 eV and align with the A, B, C, and D excitonic resonances, respectively, which can be observed in the steady-state absorption spectra of the WS_2 monolayer [24,26,38,39] (cf. Sec. S1 of the Supplemental Material [40]). Figure 1(b) shows the origin of these features. The AX and the BX are located in the K valleys in the band structure of the WS_2 monolayer. The energy difference between the two excitons is primarily attributed to spin–orbit coupling, which splits the valence band (VB) into two subbands. Besides the band edge excitons, C and D excitons are higher-lying optical transitions that form a bound state at the band nesting region along the Γ– K point and Γ point, respectively [38]. Thus, our probe can observe several excitonic resonances simultaneously. In this paper, we focus on the AX and the BX; the BX will

be shown to be a convenient observer of the EMT. Before analyzing the charge-carrier dynamics that induce the changes to the optical absorption, it is necessary to determine the initial excitation density n_0 in the system for each pump laser fluence. n_0 is determined by how many photons are absorbed in the monolayer. In the linear limit (i.e., at low laser fluences), the absorptance at the pump wavelength can be determined by steady-state spectroscopy [24]. However, strong photoexcitation can lead to changes in the absorption, as we have just demonstrated in the above exemplary dataset [see Fig. 1(c)]. To quantify the pump-induced absorption change at the pump wavelength, we integrate the differential absorption signal around the AX resonance (1.8 to 2.1 eV), computing a band integral [41] and inspect it as a function of pump laser fluence. Here and in the rest of the paper, we restrict our analysis to delays larger than 200 fs to avoid artifacts resulting from the coherences during the pump-probe overlap. Figure 1(d) shows the band integral of the AX at 200 fs relative to its steady-state value. The absorption decreases increasingly with pump fluence (note the flipped sign as indicated in the axis label). The bleach grows nonlinearly, approaching 60% at the highest pump laser fluence of 5 mJ/cm^2. The solid line is a fit with the saturable absorber model

$$I(F) = \alpha \frac{F}{F + F_{\text{sat}}}, \tag{2}$$

where α is the saturation amplitude. F_{sat} is the characteristic fluence at which the absorption reaches half of its saturated value. The fit clearly describes the trend of the AX band integral well.

The resolved trend can now be used to calculate the excitation density n_0. The band integral I is assumed to be proportional to the excitation density n_0, because of ground-state bleach as discussed below. The proportionality constant between I and n_0 can be determined by comparing the low fluence limit of Eq. (2) to the value determined from the steady-state absorptance.

The resulting excitation density as a function of laser fluence is given on the right axis in Fig. 1(d). The excitation density range of 7.75 to 43 $\times$ 10^{12} cm^{-2} covers the theoretically calculated Mott density of 8 $\times$ 10^{12} cm^{-2} for WS_2 on SiO_2 [13].

The gradual increase of the bleach of the excitonic absorption is in agreement with previous measurements of Ref. [12]. Physically, this change could be attributed to (i) ground-state bleach, (ii) changes in screening in the system (particularly upon undergoing the EMT), or (iii) pump-induced temperature changes. The latter is a weak contribution, as we show below by analyzing the kinetics of the AX band integral. The fact that the saturable absorber model fits so well to the data strongly suggests that a simple population-induced bleach is at the origin of the oscillator strength reduction. Indeed, it can be noted that up to 100% bleach is reached at high fluence and close to time zero (cf. Sec. S5 of the Supplemental Material [40]), as expected for a few-level system at population saturation. Screening, instead, does not appear to contribute to the AX bleach, and will be discussed in more detail at the end of the paper after having presented the discontinuous EMT.

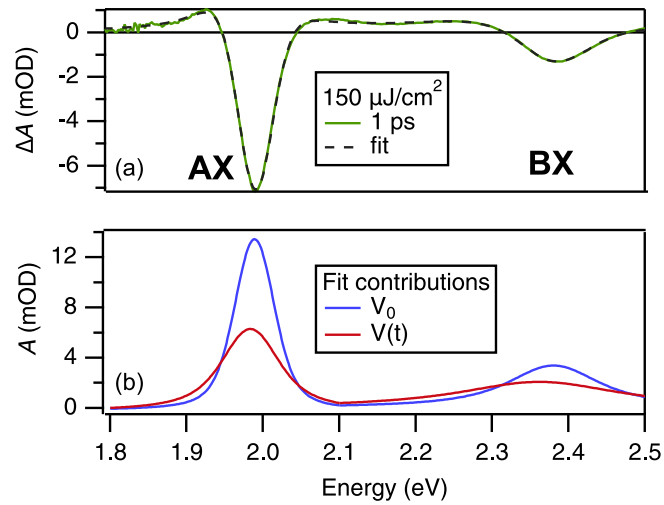


FIG. 2. (a) Differential absorption spectrum, at a delay of 1 ps and a pump fluence of 150 μJ/cm^2 ($n_0 = 15.5 \times 10^{12}$ cm^{-2}), fitted with the difference of two Voigt functions $V(t) - V_0$ [according to Eq. (3)]. (b) $V(t)$ and V_0 contribution of the fit.

B. Lineshape analysis and kinetics

After introducing the observables and determining the excitation density, we now move on to analyze the kinetics. Changes in the optical absorption of TMDC monolayers result not only from a change in the oscillator strength of excitonic resonances, but also, to a great extent, from shifts and broadening of these resonances [24,25,42]. Access to these observables requires an approach beyond spectral integration, namely lineshape analysis. In the following, we introduce our lineshape analysis model and apply it to the differential absorption data. We then proceed to analyze the kinetics of the pump-induced changes. To disentangle effects that simply scale with the number of excited quasiparticles from those that depend on their character (excitonic vs free carrier) as well as the pump-induced lattice heating, we first determine the quasiparticle population lifetime. Finally, we examine the excitonic regime and the changes of the kinetics across the Mott density.

1. Model for lineshape analysis

Figure 2(a) shows an exemplary differential absorption spectrum of the AX and the BX at a pump-probe delay of 1 ps, extracted from the two-dimensional dataset in Fig. 1(c). The shape is characterized by strong negative signals at the resonances, but also contains positive signals, which are clearly visible at the low energy side of the AX and in between the AX and the BX. As a first approximation to model the data, we assume that the differential spectrum is solely arising from a pump-induced modification of the ground-state exciton resonances. The steady-state resonances are described by Voigt profiles (cf. Sec. S1 of the Supplemental Material [40]). We therefore model the differential spectra as the difference between Voigt profiles,

$$\Delta A = V(t) - V_0. \tag{3}$$

Note that V_0 is not equal to the steady-state response V_s as discussed below. $V(t)$ and V_0 are composed of the sum of the

Voigt profiles of the AX and the BX,

$$V = V_A(S_A, \gamma_A, \sigma_A, E_A) + V_B(S_B, \gamma_B, \sigma_B, E_B). \quad (4)$$

Here, $S_{A/B}$ is the oscillator strength, $\gamma_{A/B}$ the respective Lorentzian width, $\sigma_{A/B}$ the Gaussian width, and $E_{A/B}$ are the AX and BX peak positions. For $V(t)$ the parameters are dependent on the pump-probe delay t and for V_0 they are kept the same for all delays. It should be noted that the Voigt profile is the convolution of a Gaussian and a Lorentzian profile and therefore has two width parameters. Because the difference between the two widths is very subtle and prevents convergence, a common and time-independent Gaussian width ($\sigma_{A/B} = \sigma$) for both AX and BX is used, and σ of $V(t)$ and V_0 are set equal. To describe the differential absorption data, it is sufficient to vary the Lorentzian width ($\gamma_{A/B}$) of $V(t)$ with respect to V_0.

Applying this model to fit the exemplary differential spectrum in Fig. 2(a) leads to a satisfactory match with the data. The corresponding $V(t)$ and V_0 are shown in Fig. 2(b). Before interpreting the results, i.e., the extracted nonequilibrium response $V(t)$, it is important to understand the V_0 contribution. V_0 does not vary as a function of pump-probe delay, but is extracted for each pump fluence using a global fitting procedure, in which several spectra from 200 fs to 1 ps are fitted using Eq. (3) with a common V_0 and a time varying $V(t)$. The position and width of the global fit-extracted V_0, although showing only a small variation with pump fluence, agree closely with those of the steady-state absorption (cf. Sec. S2 of the Supplemental Material [40]). However, its oscillator strength increases monotonically with pump-laser fluence (cf. Sec. S2 of the Supplemental Material [40]), and approaches the absorption in the steady state, but always remains below it. This is reasonable if one considers that a great part of the sample remains unexcited at low fluences. In the differential absorption signal ΔA as defined in the experimental section, the parts of the optical response cancel out if they are not modulated by the pump laser beam. Therefore, at low pump fluences, the oscillator strength of V_0 is expected to be lower than the steady-state value (i.e., the oscillator strength of V_s). As the pump laser fluence increases, so does the excitation density, until almost every probe photon encounters a spot that is affected by photoexcitation with the pump laser beam. This photoselection effect is reflected in the growth of V_0 with pump laser fluence. We expect, and observe, that the V_0 oscillator strength asymptotically approaches the steady-state value. We emphasize that replacing the V_0 with the known steady-state spectra of the monolayer using their full oscillator strength does not fit the differential data well. In contrast, the description of the differential data with the V_0 determined by the global fitting procedure, is excellent across a broad range of delays and fluences (cf. Sec. S3 of the Supplemental Material [40]), strongly supporting this way of analyzing the data.

By fitting $V(t)$ at all pump-probe delays with a common V_0, the following transient parameters are extracted:

$$\Delta E_{A,B}(t) = E_{A,B}(t) - E^0_{A,B},$$
$$\Delta \gamma_{A,B}(t) = \gamma_{A,B}(t) - \gamma^0_{A,B},$$
$$\Delta S_{A,B}(t) = \left(S_{A,B}(t) - S^0_{A,B}\right)/S^0_{A,B},$$

TABLE I. Fit-retrieved transient shift, broadening, and oscillator strength change of the AX and BX at a pump-probe delay of 1 ps and a pump fluence of 150 μJ/cm^2 ($n_0 = 15.5 \times 10^{12}$ cm^{-2}).

Excitonic resonance	$\Delta E_{A,B}$ (meV)	$\Delta \gamma_{A,B}$ (meV)	$\Delta S_{A,B}$ (%)
AX	-5.4 ± 0.1	39.5 ± 0.2	-21 ± 0.3
BX	-18 ± 0.9	119.0 ± 1.5	12.8 ± 0.8

where $\Delta E_{A,B}$, $\Delta \gamma_{A,B}$, and $\Delta S_{A,B}$ correspond to the transient shift, broadening, and oscillator strength change of each excitonic resonance (A, B), respectively. For the exemplary fit in Fig. 2(b), the fit retrieved shift, broadening and changes in oscillator strength magnitudes are tabulated in Table I. $V(t)$ is slightly red shifted with respect to V_0, substantially broadened, and, in the case of the AX, it also has a lower oscillator strength. The oscillator strength of BX is slightly increased, opposite to that of AX and contrary to the initial expectations from inspecting the data. We note in passing that this calls into question previous interpretations of absorption data, in which the reduction of signal at the BX energy is attributed to a reduction in its oscillator strength, because of, for example, an AX to BX population transfer [29–31,43]. Discussing the BX oscillator strength in greater detail, however, is beyond the scope of this article. Instead, we now apply the model to explore the population lifetime of A excitons, and thereafter the shift and broadening kinetics in the excitonic regime and across the Mott transition.

2. Population lifetime

In Sec. III A, we have established that the AX oscillator strength reduction is caused by ground-state bleach. We now examine the quasiparticle population lifetime by inspecting the recovery dynamics. We use the oscillator strength determined with the lineshape analysis. Almost identical results are achieved from analyzing the AX band integral kinetics (not shown).

Figure 3 shows the time-dependent oscillator strength change of the AX for different initial excitation densities. The intensity transients are normalized at 200 fs and displayed on a logarithmic scale. The oscillator strength change recovers to about 10% within the first 5 ps for all excitation densities—slightly slower for the lowest and slightly faster for the highest excitation density. The remaining 10% decays on a tens-of-picoseconds timescale (not shown) and is attributed to pump-induced lattice heating, which cools on a 20–30-ps timescale, as established in the subsequent section.

To extract the population lifetime, we fit the data using a single exponential decay function,

$$y(t) = A_{\text{pop}} \exp(-t/\tau_{\text{pop}}) + y_0, \quad (5)$$

with the population decay time constant (τ_{pop}) and an offset y_0 accounting for the remaining oscillator strength bleach. The fit describes the data well. At an excitation density of 15.5×10^{12} cm^{-2}, a dataset that we analyze in detail in the next section, the extracted population lifetime is $\tau_{\text{pop}} = 1.4 \pm 0.2$ ps. For the highest excitation density, the lifetime reduces to $\tau_{\text{pop}} = 1.1 \pm 0.2$ ps. These values are in the range

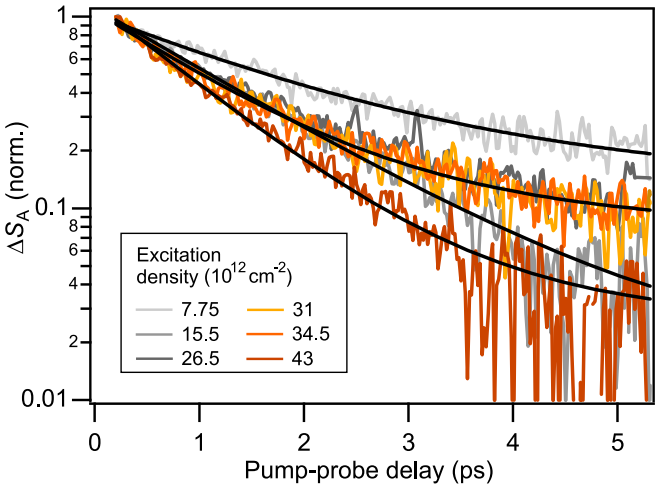


FIG. 3. Ultrafast relaxation of the AX oscillator strength change, i.e., the ground-state bleach, for different initial excitation densities. To evaluate the relaxation time, the traces are normalized at 200 fs and fitted with a single-exponential decay function (see text). For clarity, the fit functions are shown only for four traces, as black lines.

of those determined with time-resolved photoelectron spectroscopy measurements at room temperature [44] as well as other optical studies at comparable excitation densities [45]. From the above, we have determined the population lifetime. This enables us to interpret the shift and broadening kinetics in the following.

3. *Excitonic regime*

We start by characterizing the optical response in the excitonic regime before proceeding to high excitation densities at which the Mott transition occurs. We inspect the peak shifts and width changes of the AX and the BX as a function of pump-probe delay for a low excitation density of 15.5×10^{12} cm^{-2}. As outlined in the Introduction, based on previous experimental findings [24,25] and theoretical predictions [32], we expect a blue shift of the AX in the presence of A excitons but not of the BX. Furthermore, we expect a red shift of both the AX and the BX because of the pump-induced lattice heating, which causes BGR. In addition, both population and pump-induced lattice heating are expected to lead to broadening [24,46–49]. In a collisional broadening picture, this should affect both excitonic resonances simultaneously. It should be noted that excitons and phonons (as well as free carriers that will be formed at higher excitation densities) are individual sets of quasiparticles, each evolving with their specific time constants. The observables, i.e., the optical resonances, reflect the superposition of the effects of all quasiparticles. We will show in this section empirically that all kinetics can be described with the superposition of exponential decays, each accounting for the temporal evolution of one set of quasiparticles. Based on this, we will develop a global fit function in the next section that works across all excitation densities and delays. This will allow us to disentangle the contributions of excitons, free carriers and lattice heating to the optical response across the Mott density.

Figure 4(a) shows the overall shift of the AX resonance. Prior to going through the description of the dynamics in detail, let us note that we refer to shift components with a positive amplitude as "blue shifts" and those with a negative amplitude as "red shifts." Because the measured dynamics arise from the superposition of multiple components with different decay constants, the overall shift at a given pump–probe delay may be either red or blue. In particular, a rapidly decaying initial blue shift superimposed on a more slowly decaying red shift can produce the appearance of a rising red shift (and vice versa).

The overall AX shift firstly (at 200 fs) exhibits a few meV blue shift ($\Delta E_A > 0$), which decays quickly. This is followed by the apparent rise of a red shift on a timescale of a few picoseconds and, finally, equilibration dynamics on a

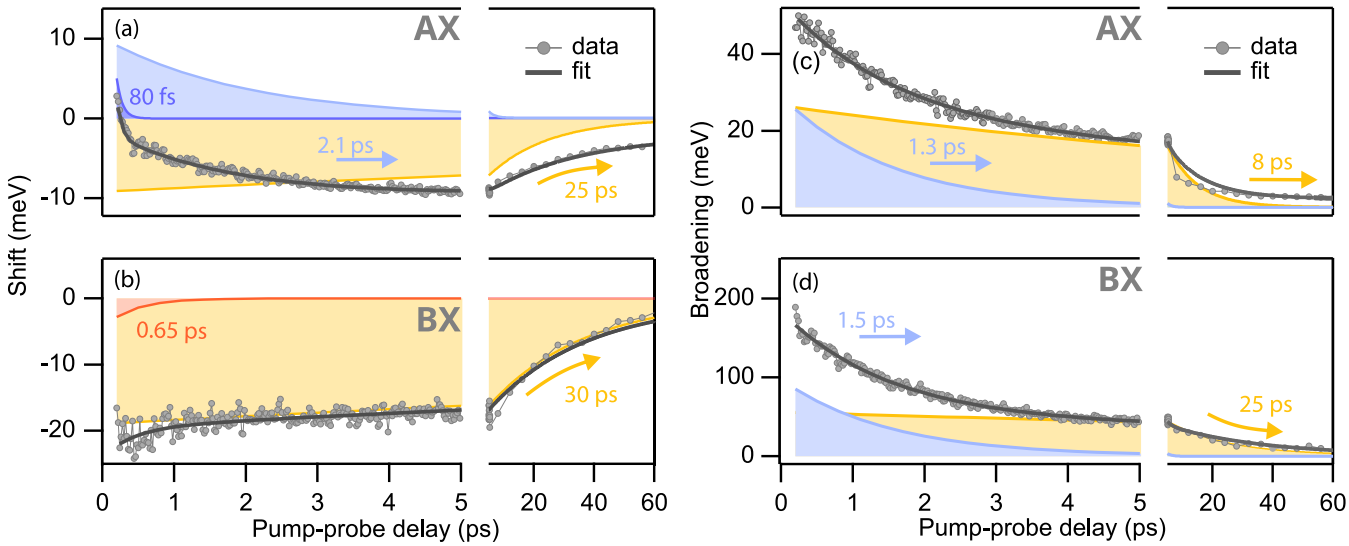


FIG. 4. Shift (a), (b) and broadening (c), (d) of A and B exciton resonances at a low excitation density (15.5×10^{12} cm^{-2}) as a function of pump-probe delay. The data are fitted with a sum of exponential decay functions as described in the text. The individual components of the fit are illustrated with the shaded areas.

tens-of-picoseconds timescale. We find that the observed dynamics of the AX shift can be best fitted with a sum of three exponential decay functions, with two blue shift components and one red shift component, plus an offset. In preparation for the global fit developed later, we write

$$\Delta E_{\mathrm{A}}(t) = B_0\, e^{-t/\tau_0} + B_1\, e^{-t/\tau_1} + R\, e^{-t/\tau_2} + y_0. \quad (6)$$

The resulting fit is shown as a black solid line on top of the data in Fig. 4(a). It describes the data well. The figure also contains a decomposition of the total fit function into the contribution of each exponential to the fit (blue and orange curves). For the AX shift, the main part of the observed dynamics can be described with a blue shift decaying with $\tau_1 = 2.1 \pm 0.1$ ps plus a red shift decaying with $\tau_2 = 25 \pm 1$ ps. In addition, there is a very small contribution of a blue shift at early time delays decaying with $\tau_0 = 80 \pm 10$ fs as well as a longer-lived signal, captured by y_0. τ_1 is close to the population lifetime $\tau_{\mathrm{pop}} = 1.4 \pm 0.2$ ps established from the ground-state bleach recovery in the preceding section. τ_2 is in agreement with the cooling time constant τ_{cool} of several tens of picoseconds resolved in previous work [24,25]. These two contributions are therefore attributed to an A exciton population-induced blue shift and the lattice heating-induced BGR, respectively. The lattice heating-induced red-shift amplitude R is determined to be -18.3 ± 0.1 meV, which is in agreement with the value reported in Ref. [25] at a similar pump fluence. Using a proportionality constant derived from equilibrium measurements, see Ref. [25] and references therein, we can estimate that the pump excitation at this fluence leads to an increase in lattice temperature by 30 K at time zero. Beyond these two contributions, the extracted decay time constant of the small initial blue shift is in agreement with the scattering time constant of K-valley electrons into the Σ Valley at the center of the Brillouin zone [50,51]. We refer to it as τ_Σ in the following. The remaining signal after 60 ps, captured by y_0 with the fit is commensurate with lifetimes of defect-trapped carriers, which range up to ns [52,53]. As the τ_Σ blue shift component and the remaining signal arising from defects are essentially out of the range of recorded delays, we do not discuss them further. Overall, as expected for the excitonic regime, the decay dynamics are dominated by the pump-induced excitons and lattice heating, each following first-order kinetics. The two contributions can be well separated, both because of their different timescales and because they induce shifts of opposite sign: In the main section of the accessed delay window, the AX shift dynamics are the superposition of a blue shift arising from the A exciton population decaying with τ_{pop} and a red shift arising from pump-induced lattice heating decaying with τ_{cool} on a tens of picoseconds timescale.

We now turn to the BX shift. As shown in Fig. 4(b) it exhibits a red shift of −20 meV at 200 fs. Except for a very small part of the red shift that decays in the first picoseconds, relaxation takes place on a timescale of tens of picoseconds. We find that the BX shift is best described with the sum of two exponential decay functions, with two red shift components. Again, as preparation for the global fit employed later, we write this down explicitly

$$\Delta E_{\mathrm{B}}(t) = R_1\, e^{-t/\tau_1} + R_2\, e^{-t/\tau_2}. \quad (7)$$

The resulting fit is shown as a black solid line on top of the data in Fig. 4(b). The decomposition of the fit function into the individual components (solid red and yellow lines with shaded area) reveals that the main part of the BX red shift relaxes with a time constant of $\tau_2 = 30 \pm 1$ ps to the equilibrium, in agreement with τ_{cool}, the lattice cooling time constant established above. A very small part of the shift ($R_1 = -2$ meV) relaxes with a time constant of $\tau_1 = 0.65 \pm 0.10$ ps. This is much faster than the population relaxation time constant $\tau_{\mathrm{pop}} = 1.4 \pm 0.2$ ps. As shown below for the region above the Mott limit, τ_1 can be related to the decay of free carriers. A small population of free carriers has been detected before in the low excitation density regime and has been attributed to defect-ionized excitons [15]. Remarkably, the BX exhibits no component decaying on the timescale of the population decay. This contrasts with the AX but agrees with theoretical predictions [32]. It is the absence of BX shift dynamics on timescales of a few picoseconds that allows the detection of a very small contribution of the free carrier population, which would likely be obscured otherwise.

To further corroborate that the dynamics in the excitonic regime are dominated by the pump-induced excitons and lattice heating, we also inspect the broadening. The broadening for the AX and the BX is shown in Figs. 4(c) and 4(d). Both excitonic resonances are already broadened at 200 fs and the broadening relaxes on a picosecond timescale. Fits with a biexponential decay are shown as black solid lines for both panels. They clearly describe the data well. The resulting time constants are $\tau_1 = 1.3 \pm 0.1$ ps, $\tau_2 = 8 \pm 1$ ps for the AX, and $\tau_1 = 1.5 \pm 0.1$ ps, $\tau_2 = 25 \pm 1$ ps for the BX. These two time constants agree well with τ_{pop} and τ_{cool} established above. The finding that τ_1 equals τ_{pop} implies a proportionality between broadening and exciton population, in agreement with previous reports [24,48,49,54].

Taken together, shift and broadening kinetics in the excitonic regime can be largely attributed to pump-induced A excitons and pump-induced lattice heating as observed in previous studies. The decay of the pump-induced changes can be described empirically with a sum of exponential decay functions, each accounting for different processes in the sample that superimpose to a total shift and broadening of the excitonic resonances, respectively. Notably, the BX shift is, on the one hand, insensitive to the A exciton population as predicted theoretically [32]. On the other hand, it is sensitive to changes in the underlying single-particle band structure through BGR induced by lattice heating and free carriers. These properties qualify the BX resonance to be a spectator of the Mott transition.

4. Exciton Mott transition

Upon increasing the excitation density and crossing the Mott density, photoexcitation will initially still create A excitons, but they subsequently dissociate into free carriers, i.e., an electron–hole plasma. The electron–hole plasma induces BGR and is expected to red shift the excitonic resonances [24]. We restrict the discussion here to the AX and the BX shift. The broadening also shows strong changes at the same excitation density [55] (cf. Sec. S7 of the Supplemental Material [40]). A detailed discussion is beyond the scope of

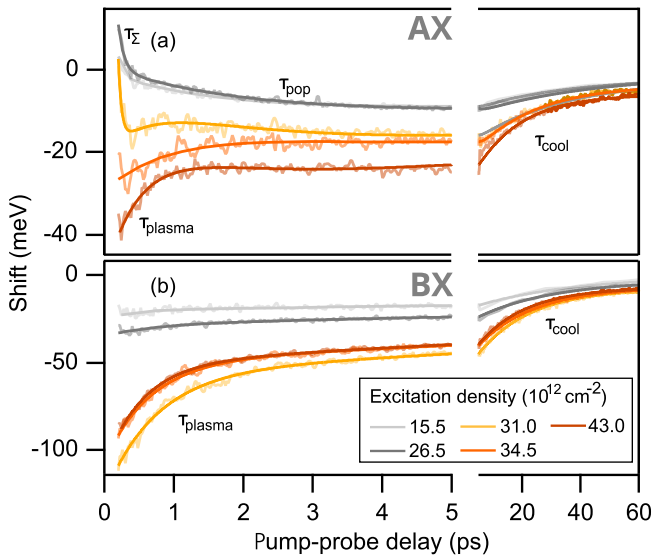


FIG. 5. AX (a) and BX (b) shifts as a function of pump-probe delay for different initial excitation densities, together with fits (solid lines). The fit functions are the sum of four and two exponential decays for AX [see Eq. (14)] and BX [see Eq. (13)], respectively.

the present publication. For the shift analysis presented in the following, it should be noted that the dissociation is expected to happen on a screening timescale of tens of femtoseconds as mentioned in the Introduction [21]. Since we only analyze pump-probe delays >200 fs, we expect to observe only the decay and not the formation of the plasma.

Figure 5 shows the AX and the BX shift as a function of pump-probe delay for different excitation densities. The low excitation density trace at 15.5×10^{12} cm^{-2} discussed in the last section is shown in light gray as a reference. Roughly doubling the excitation density does not change the dynamics qualitatively, neither for the AX [Fig. 5(a)] nor for the BX [Fig. 5(b)].

However, already at a slightly higher excitation density of 31×10^{12} cm^{-2}, the dynamics change dramatically: the corresponding yellow trace shifts down, up, down, and up again with various timescales. As will be clear later on, this is caused by the superposition of multiple peak shifts caused by different physical phenomena. At an excitation density of 31×10^{12} cm^{-2}, the shifts, coincidentally, have comparable amplitudes. Even higher excitation densities result in a clear initial red shift of −30 to −40 meV, which partially decays within ca. 1 ps. After this initial relaxation, the dynamics show a similar decay as for low excitation densities.

At the same critical excitation density of 31×10^{12} cm^{-2}, the initial red shift of the BX jumps abruptly from −30 meV to about −100 meV. For even higher excitation densities the initial red shift does not increase further. The enhanced initial red shift decays with ca. 1 ps. After this initial relaxation, the dynamics also show a similar decay as for low excitation densities, i.e., a red shift that decays into equilibrium on a timescale of tens of picoseconds.

Note that the abrupt red shift is also visible in the raw data: See Sec. S4 of the Supplemental Material [40] for a comparison of the spectra below and across the critical excitation density, together with a demonstration of how the lineshape analysis captures the spectral changes.

The abrupt appearance of an enhanced red shift in both excitonic resonances, which quickly decays with a similar rate, strongly suggests that the excitation density has crossed the Mott limit. The pump laser beam now creates a sufficiently large excitation density, such that initially excited excitons dissociate into free carriers. This apparently happens within less than 200 fs and induces a red shift of both excitonic resonances through BGR. The red shift decays within a picosecond and is followed by shift dynamics similar to those in the low-excitation-density regime. In particular, the AX shift also shows a weak few-ps blue shift contribution as τ_1 in the previous Sec. III B3 that was attributed to the exciton population decay [τ_{pop} component, cf. gray traces and yellow trace in Fig. 5(a)]. This indicates the decay of the plasma and subsequent re-establishment of the excitonic phase.

In the following, we develop a fit model that allows us to describe the peak shifts quantitatively. It is based on three contributions, i.e., lattice heating, excitons, and the plasma. We will prepare for a global fit across all excitation densities and delays to determine the time constant associated with the decay of the plasma phase and follow the evolution of the plasma as a function of excitation density. This will finally allow us to discuss the character of the transition.

The basic assumption for the fit model is that the plasma population (n_{plasma}) either builds up an exciton population (n_{AX}) and then subsequently recombines, or directly decays into the ground state by recombination. This can be represented as the following coupled rate equations:

$$\frac{dn_{\mathrm{plasma}}}{dt} = -\frac{1}{\tau_{\mathrm{AX}}} n_{\mathrm{plasma}} - \frac{1}{\tau_{\mathrm{pop}}} n_{\mathrm{plasma}}, \tag{8}$$

$$\frac{dn_{\mathrm{AX}}}{dt} = \frac{1}{\tau_{\mathrm{AX}}} n_{\mathrm{plasma}} - \frac{1}{\tau_{\mathrm{pop}}} n_{\mathrm{AX}}. \tag{9}$$

The excitons and free charge carriers are assumed to have the same recombination time constant τ_{pop}, which is justified empirically as the ground-state bleach recovery changes only slightly as a function of excitation density (cf. Fig. 3). The solution of the rate equation system is

$$n_{\mathrm{plasma}}(t) = n^0_{\mathrm{plasma}} \mathrm{e}^{-\frac{t}{\tau_{\mathrm{plasma}}}}, \tag{10}$$

$$n_{\mathrm{AX}}(t) = \left[n^0_{\mathrm{plasma}}(1 - \mathrm{e}^{-\frac{t}{\tau_{\mathrm{AX}}}}) + n^0_{\mathrm{AX}}\right] \mathrm{e}^{-\frac{t}{\tau_{\mathrm{pop}}}} \tag{11}$$

with

$$\tau_{\mathrm{plasma}} = \left(\frac{1}{\tau_{\mathrm{AX}}} + \frac{1}{\tau_{\mathrm{pop}}}\right)^{-1}, \tag{12}$$

n^0_{plasma} is the initial plasma population directly after the dissociation process. n^0_{AX} is the exciton population that remains from the dissociation process. Incorporating this is necessary to cover the case of the low-excitation-density regime, where n^0_{AX} dominates. Furthermore, we can cover the cases of a discontinuous or continuous Mott transition, where the pump-induced A excitons are dissociated completely at the Mott density or to a continuously increasing fraction upon increasing the excitation density, respectively.

We now deduce fit functions for our observables, namely the AX and the BX shift, based on the rate equation model above and incorporating the additional contributions to the AX and BX shift derived with the empirical fits in the last section. We assume that the plasma population leads to BGR and hence a red shift of both the AX and the BX, proportional to n_{plasma}. Furthermore, the AX (but not the BX) exhibits a blue shift proportional to n_{AX}. As established in the last section, pump-induced lattice heating leads to an additional red shift contribution of both excitonic resonances, which decays exponentially in time with τ_{cool}. With this, the fit function of the BX shift becomes a sum of two exponential decays,

$$\Delta E_{\mathrm{B}}(t) = R^{\mathrm{B}}_{\mathrm{plasma}} \mathrm{e}^{-t/\tau_{\mathrm{plasma}}} + R^{\mathrm{B}}_{\mathrm{heat}} \mathrm{e}^{-t/\tau_{\mathrm{cool}}}. \tag{13}$$

Here, $R^{\mathrm{B}}_{\mathrm{plasma}}$ and $R^{\mathrm{B}}_{\mathrm{heat}}$ are the plasma and lattice-temperature-induced red-shift amplitudes, respectively. $R^{\mathrm{B}}_{\mathrm{plasma}}$ is proportional to the initial plasma population n^0_{plasma} via Eq. (10). This fit function is identical to the one derived empirically in the previous section [cf. Eq. (7)] to describe the dynamics in the excitonic regime. This enables systematic tracking of the shift amplitudes over the entire excitation density range below.

The fit function for the AX shift has three more components because of the sensitivity to the AX population n_{AX}, an additional fast ($\tau_\Sigma = 80$ fs) decaying blue shift at early delays [56] and a long-lived component y_0; cf. the previous section. This leads to a sum of four exponential decays associated with τ_{plasma}, τ_{pop}, τ_{cool}, and τ_Σ, plus an offset,

$$\Delta E_{\mathrm{A}} = R^{\mathrm{A}}_{\mathrm{plasma}} \mathrm{e}^{-t/\tau_{\mathrm{plasma}}} + B^{\mathrm{A}}_{\mathrm{pop}} \mathrm{e}^{-t/\tau_{\mathrm{pop}}} + R^{\mathrm{A}}_{\mathrm{heat}} \mathrm{e}^{-t/\tau_{\mathrm{cool}}} + B^{\mathrm{A}}_{\Sigma} \mathrm{e}^{-t/\tau_\Sigma} + y_0. \tag{14}$$

Here, $R^{\mathrm{A}}_{\mathrm{plasma}}$ and $R^{\mathrm{A}}_{\mathrm{heat}}$ are the plasma and lattice temperature-induced red-shift amplitude, respectively. As for the BX shift, $R^{\mathrm{A}}_{\mathrm{plasma}}$ is proportional to the initial plasma population n^0_{plasma}, which enters via Eqs. (10) and (11). $B^{\mathrm{A}}_{\mathrm{pop}}$ is a blue shift caused by the A exciton population term Eq. (11). Not trivially though, it is proportional to the sum of n^0_{plasma} and n^0_{AX}, which is equal to the total pump-induced excitation density. This is because the model assumes that the plasma decays partially by forming A excitons. This exciton population then blue shifts the AX resonance the same way as initially created excitons do. Compared to the empirical fit in the previous section, which perfectly described the dynamics in the excitonic regime, an additional exponential decay is introduced to describe the plasma-induced red shift $R^{\mathrm{A}}_{\mathrm{plasma}}$. This is forced to be zero at low excitation densities to avoid overfitting.

We now fit the shifts for both the AX and the BX by optimizing τ_{plasma} and τ_{cool} globally across all excitation densities and together for the AX and the BX shift. Here, τ_{pop} is determined from the ground-state bleach recovery of the AX (Sec. III B2). τ_Σ is fixed at 80 fs. The fits are shown with the solid lines in Fig. 5. Clearly, they describe the peak shifts for both excitonic resonances well. The retrieved plasma decay time is $\tau_{\mathrm{plasma}} = 0.65 \pm 0.1$ ps. The good match of the fit for both the AX and the BX shift using globally determined time constants shows that the peak shifts can be described with only three coupled contributions, i.e., the temporal evolution of lattice heating, excitons and the plasma. In particular, the global fit shows that the initial red shift observed in both excitonic resonances at elevated excitation densities decays with the same rate. It therefore must be of the same physical origin, consistent with a plasma population causing BGR, which affects both excitonic resonances. Notably, τ_{plasma} agrees well with the decay time of stimulated emission from plasma carriers in the renormalized conduction band, observed in optical spectroscopy at high excitation densities for the same sample system [12].

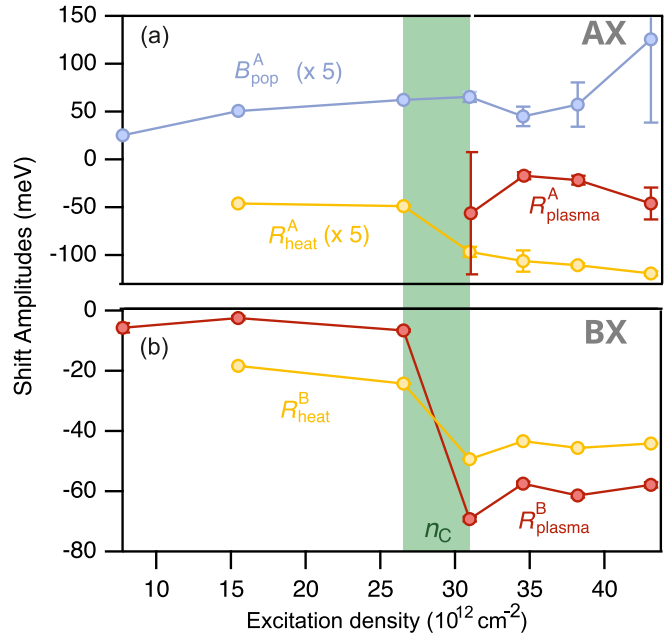


FIG. 6. Shift amplitudes associated with the three decay time constants τ_{pop}, τ_{cool}, and τ_{plasma} (see text) for both AX (a) and BX (b) as functions of excitation density. $B^{\mathrm{A}}_{\mathrm{pop}}$ and $R^{\mathrm{A}}_{\mathrm{heat}}$ are multiplied by a factor of 5 to display the trend more clearly. The jump of all amplitudes except $B^{\mathrm{A}}_{\mathrm{pop}}$ across the Mott density (n_C) indicates a discontinuous Mott transition.

Having established that the excitonic resonances detect a plasma and its decay at elevated excitation densities, we now tackle the question of whether the dissociation ratio, and hence the plasma population, increases discontinuously or continuously upon increasing the excitation density. Clearly, in the time domain, a continuous decay of the plasma population is observed, leading to a gradual relaxation of the plasma-induced red shift for both the AX and the BX shift with τ_{plasma} and the reestablishment of the excitonic regime. This behavior is independent of the character of the phase transition, because the plasma population decay is based on probabilistic events and not an abrupt coherent process such as optical excitation. To investigate the pump-induced effects extrapolated to the moment immediately after the dissociation, we inspect the relevant shift amplitudes as a function of initial excitation density. These are shown in Fig. 6 for the AX and the BX, respectively. We can distinguish the following trends:

(1) The population-induced blue-shift amplitude of the AX $B^{\mathrm{A}}_{\mathrm{pop}}$ (blue) increases as a function of excitation density.

(2) The plasma-induced red-shift amplitude of the AX $R^{\mathrm{A}}_{\mathrm{plasma}}$ (red, top), which can only be resolved above 31×10^{12} cm^{-2}, is at about -30 to -50 meV above this excitation density.

(3) The plasma-induced red-shift amplitude of the BX R^{B}_{plasma} (red, bottom) is very small but finite below 31×10^{12} cm^{-2} and then jumps to -70 meV. It stays almost constant thereafter.

(4) The lattice-heating induced red-shift amplitudes of the AX and BX, i.e., R^{A}_{heat} and R^{B}_{heat} (orange), increase as a function of excitation density, but exhibit a distinct jump between 26.5×10^{12} cm^{-2} and 31×10^{12} cm^{-2}.

All shift components besides B^{A}_{pop} exhibit an abrupt change upon increasing the excitation density from 26.5×10^{12} cm^{-2} to 31×10^{12} cm^{-2}. We thus define a critical density $n_C = 29 \pm 2 \times 10^{12}$ cm^{-2} (green shaded area in Fig. 6). At n_C, a fundamental change in the kinetics occurs, showing that it separates two distinct phases of the system. In particular, the simultaneous and abrupt increase of the plasma-induced AX and BX red-shift amplitudes R^{A}_{plasma} and R^{B}_{plasma} is consistent with a Mott transition occurring at n_C. Whether or not this transition is of continuous or discontinuous character is discussed in the following.

As outlined above, the red-shift amplitudes R^{A}_{plasma} and R^{B}_{plasma} are proportional to the plasma population after the initial dissociation process of pump-induced A excitons. In the low-excitation-density regime below n_C, only a few excitons dissociate. The plasma-induced red-shift amplitudes therefore are expected to be small. This agrees well with the observation that the AX red shift R^{A}_{plasma} can only be resolved above n_C. Because of the overlapping blue shift of the AX caused by the A exciton population (which likely also leads to the high error bars in the R^{A}_{plasma} and B^{A}_{pop} amplitudes above n_C), a small plasma-induced red shift evolving at a similar time scale as the overall quasiparticle population decay with τ_{pop} is invisible. Notably, the BX red-shift amplitude R^{B}_{plasma} remains small but finite for all excitation densities below n_C. This observation shows, consistent with the individual fits in the preceding section, that in the excitonic regime a small plasma population is formed. The BX shift serves as an exclusive spectator of BGR and therefore allows us to resolve the plasma-induced red shift across all excitation densities.

At the Mott density, exciton dissociation becomes favorable. The dissociation ratio, i.e., the plasma population compared to the total excitation density, is expected to change. Crucially, the change of the BX red-shift amplitude R^{B}_{plasma} at n_C is abrupt, reminiscent of a step function as a function of the excitation density. This indicates an equally abrupt change of the dissociation ratio at n_C. This observation strongly suggests that the Mott transition has a discontinuous character and not a continuous one, in which case we would expect that R^{B}_{plasma} changes gradually as a function of the excitation density. The sharp character of the transition is underscored by the abrupt appearance of the AX red-shift amplitude R^{A}_{plasma} at n_C. Moreover, it is substantiated by the jump of the lattice-heating-induced red-shift amplitudes R^{A}_{heat} and R^{B}_{heat} at n_C. The increased lattice heating can likely be attributed to an increased electron–phonon scattering cross section, as free carriers have an increased mobility compared to excitons. It is important to note that the increase in the AX blue-shift amplitude B^{A}_{pop} over n_C does not contradict the interpretation of a discontinuous Mott transition. As explained above, within the rate equation model the AX blue-shift amplitude B^{A}_{pop} associated with τ_{pop} is proportional to the total excitation density, which is composed of the sum of the plasma and exciton population and is independent of the dissociation ratio. We therefore expect that it does not change abruptly at the critical density, and the fact that this is not the case implicitly shows that the assumption of the rate equation model must be satisfied, i.e., that the plasma decays through the combined action of exciton formation and recombination.

Compared with theoretical predictions of plasma-induced BGR at the Mott density, the values determined here are relatively low. The experimentally determined value of the BGR by this method is, taking the BX shift as a reference, -70 meV, which is considerably lower than the theoretically calculated value of about -350 meV [13]. This is likely because the BGR is probed via an optical transition, rather than through direct measurement of electronic energies via, e.g., photoelectron spectroscopy [36]. Screening leads to a concurrent blue shift of excitonic resonances because of the reduction of the binding energy, as is known from previous studies of the excitonic regime [24]. The two effects, binding energy reduction and BGR, partially compensate for each other [57], resulting in a smaller effective red shift.

In summary, both the AX and the BX exhibit an abrupt and strong red shift at the same excitation density of $n_C = 29 \pm 2 \times 10^{12}$ cm^{-2}, which decays with the same timescale. We attribute this to free-carrier-induced BGR upon crossing the Mott density. A simple rate equation model is introduced, which assumes that the photoexcitation—besides heating the lattice—creates excitons, and for sufficiently high excitation densities, dissociated excitons, i.e., free carriers. The free carriers have two decay channels, namely recombination and exciton formation. This model describes the observed shift dynamics for both the AX and the BX very well for both the excitonic and plasma phases with globally determined time constants for the plasma decay, the population lifetime, and the lattice cooling. The global fit is quantitatively consistent with independent fits performed in the excitonic regime. The fitting enables the tracking of the amplitudes of the free-carrier-induced BGR, the lattice-heating-induced BGR, and the total pump-induced population on the excitonic resonances across all excitation densities. All these parameters (besides the total pump-induced population) show an abrupt change at the critical density.

IV. DISCUSSION AND CONCLUSIONS

The above evaluation of the broadband differential TA data through careful lineshape analysis has enabled us to discern that monolayer WS_2 exhibits two distinct regimes of photoexcited dynamics, which are separated by an abrupt change at a critical excitation density. At low excitation densities up to 26.5×10^{12} cm^{-2}, the pump-induced dynamics are dominated by excitons and lattice heating, occurring at their characteristic timescales. While lattice heating leads to a red shift through BGR that affects all excitonic resonances, the presence of A excitons uniquely impacts the AX peak position, causing it to blue shift. It does not affect the BX peak position, as theoretically predicted [32]. This independence of the BX peak position from the A exciton population makes it a spectator of even small changes in

the BGR, and the analysis shows that a small quantity of pump-induced free charge carriers must be present in the excitonic regime. At 31×10^{12} cm^{-2} and higher excitation densities, the optical spectra suddenly indicate the presence of a large number of free charge carriers. The plasma creates BGR and red shifts the lowest optical transitions, the AX and the BX likewise. As the quasiparticle density decreases with time and rapidly falls below the Mott limit, the plasma decays gradually by A exciton formation and recombination, with a time constant of 0.65 ps. The reemergence of the excitonic phase after the plasma decay is demonstrated by the recurrence of the dynamics of the excitonic phase, in particular, the A exciton population-induced blue shift of the AX.

The observation of two distinct regimes, separated by a critical excitation density, shows that the EMT in monolayer WS_2 is a sharp transition. Within an excitation density window of only 4.5×10^{12} cm^{-2} i.e., 15% of the Mott density $n_C = (29 \pm 2) \times 10^{12}$ cm^{-2}, the shift amplitude of the B exciton increases by a factor of 10. The sharpness of the jump is comparable to the calculation by Steinhoff *et al.* [13]. In both the theoretical calculation of Ref. [13] and our experiment, the sharpness is limited by the amount of data points across the critical density. This observation is in contrast to the gradual reduction of the AX oscillator strength over a broad excitation density regime observed by us and Ref. [12]. The gradual bleach is the result of a population-induced ground-state bleach, combined with a finite exciton dissociation time as discussed below. The sharp transition strongly suggests that the EMT has a discontinuous character, but it cannot be regarded as proof. We expect that even if the EMT is truly discontinuous, inhomogeneities within the excitation spot, as well as experimental parameters such as the laser power stability, would lead to a finite broadening of the jump. A finer sampling across the critical density would therefore likely not help to resolve the question fundamentally. It is noteworthy that, in our experiments, the pump spot is about the same size as the probe laser spot, as mentioned in the experimental section. This creates a macroscopic inhomogeneity of the pump laser fluence within the probe spot and is expected to broaden an initially sharp transition—the center of the Gaussian-shaped excitation spot would undergo an EMT at a lower pump laser fluence than the outer ring segments. Despite all these existing causes that would lead to an apparent broadening, our experiments show a rather sharp jump as outlined before. While we currently cannot estimate the broadening effects quantitatively, an intriguing possibility would be that the transition is in fact avalanche-like. In an avalanche-like transition, one could expect that if a sufficient part of the photoexcited area (e.g., the center of the photoexcited spot) undergoes an EMT, it will assist in dissociating excitons present in the neighboring areas that have not yet reached the Mott density [18]. To explore this further, spatial resolution could be a next step, e.g., monitoring the TA locally at the center of a Gaussian-shaped excitation spot and comparing this to an outer segment.

Our observation of a sharp EMT is in agreement with the abrupt photoluminescence change under cw laser excitation at a critical density, observed in monolayer MoS_2 and attributed to the EMT [10]. Apparently, W-based and Mo-based TMDC systems do not behave differently in this respect, despite theoretical predictions of different behavior because of their differences in exciton binding energy [14]. The finding of a sharp transition is in agreement with the material-realistic many-body theory [13]. The finite amount of plasma formed before the critical density, resolved through the BX shift, is explained by the exciton-screening induced dissociation by Steinhoff et al. [13]. Plasma formation, locally within the excited oscillator strength, could, however, also be favored via exciton dissociation at defects [15]. Notably, Mott density $n_C = 29 \pm 2 \times 10^{12}$ cm^{-2} is somewhat higher than the value of 8×10^{12} cm^{-2} predicted by Steinhoff *et al.* and is notably close to the critical density of 34×10^{12} cm^{-2} in the cw laser experiments in MoS_2. In their case, they attributed this phase to an electron–hole liquid instead of an electron–hole plasma [16]. The existence of this exotic phase in this and other studies [17] is substantiated by imaging of the photoexcited spot. This once again motivates the use of spatially resolved techniques with ultrafast time resolution to study the EMT in WS_2 could be an interesting topic for future studies.

We observe this transition in combination with the previously observed gradual bleach of the A exciton resonance as a function of excitation density [cf. Fig. 1(d)]. As explained in Sec. III A, the A exciton bleach can be entirely explained by the ground-state bleach caused by the pump-induced population. It clearly shows no abrupt change at the Mott density, which means that there is no screening-induced change of the A exciton oscillator strength. The persistence of the A and B excitonic resonances above the Mott density shows that excitons are still eigenstates of the system. This may seem inconsistent with our interpretation of a discontinuous Mott transition at first sight. However, as mentioned in the Introduction, even if an incoherent exciton population is formed, this population would be expected to dissociate and form plasma only within a screening timescale. In our case, this must have happened within 200 fs, which is also in agreement with measurements for bulk WSe_2 [19]. These findings show that simply measuring the oscillator strength of excitonic resonances as an indicator of the EMT is not sufficient. However, their shift dynamics can be used to examine the nature of the transition and the associated time constants, as we have shown.

With this study, we demonstrate the applicability of optical spectroscopy combined with a detailed lineshape analysis of the differential spectra to study Mott transitions via excitonic resonances. The sharp character of the particular Mott transition in WS_2 monolayers could be useful for photoswitches, exploiting the change in the optical or electronic properties.

ACKNOWLEDGMENT

We acknowledge Xiaoyang Zhu's continuing support of the WS_2 project.

DATA AVAILABILITY

The data analyzed in the present study are publicly available on Zenodo [60].

[1] M. Ye, D. Zhang, and Y. K. Yap, Recent advances in electronic and optoelectronic devices based on two-dimensional transition metal dichalcogenides, Electronics **6**, 43 (2017).

[2] X. Liu and M. C. Hersam, 2D materials for quantum information science, Nat. Rev. Mater. **4**, 669 (2019).

[3] S. Wu, S. Buckley, J. R. Schaibley, L. Feng, J. Yan, D. G. Mandrus, F. Hatami, W. Yao, J. Vučković, A. Majumdar, and X. Xu, Monolayer semiconductor nanocavity lasers with ultralow thresholds, Nature (London) **520**, 69 (2015).

[4] J. Wang, J. Ardelean, Y. Bai, A. Steinhoff, M. Florian, F. Jahnke, X. Xu, M. Kira, J. Hone, and X.-Y. Zhu, Optical generation of high carrier densities in 2D semiconductor heterobilayers, Sci. Adv. **5**, eaax0145 (2019).

[5] Q. Li, L. Sui, G. Niu, J. Jiang, Y. Zhang, L. Che, G. Wu, M. Jin, and K. Yuan, Ultrafast optical switching to a metallic state via photoinduced Mott transition in few-layer MoS_2 under hydrostatic pressure, Phys. Rev. B **103**, 125416 (2021).

[6] Y. Yu, G. Li, and L. Cao, Exciton Mott transition in two-dimensional semiconductors, arXiv:2007.11509.

[7] Y. Xu, Y. Xiang, M. Shi, B. Zhai, W. Dai, T. Wang, X. Liu, Y. Yu, and J. He, Room-temperature amplified spontaneous emission in two-dimensional WS_2 beyond exciton Mott transition, Phys. Rev. Lett. **134**, 066904 (2025).

[8] T. Siday, F. Sandner, S. Brem, M. Zizlsperger, R. Perea-Causin, F. Schiegl, S. Nerreter, M. Plankl, P. Merkl, F. Mooshammer, M. A. Huber, E. Malic, and R. Huber, Ultrafast nanoscopy of high-density exciton phases in WSe_2, Nano Lett. **22**, 2561 (2022).

[9] P. L. Pekh, P. V. Ratnikov, and A. P. Silin, Electron-hole liquid in monolayer transition metal dichalcogenide heterostructures, JETP Lett. **111**, 90 (2020).

[10] A. W. Bataller, R. A. Younts, A. Rustagi, Y. Yu, H. Ardekani, A. Kemper, L. Cao, and K. Gundogdu, Dense electron–hole plasma formation and ultralong charge lifetime in monolayer MoS_2 via material tuning, Nano Lett. **19**, 1104 (2019).

[11] F. B. Sousa, R. Perea-Causin, S. Hartmann, L. Lafetá, B. Rosa, S. Brem, C. Palekar, S. Reitzenstein, A. Hartschuh, E. Malic, and L. M. Malard, Ultrafast hot electron–hole plasma photoluminescence in two-dimensional semiconductors, Nanoscale **15**, 7154 (2023).

[12] A. Chernikov, C. Ruppert, H. M. Hill, A. F. Rigosi, and T. F. Heinz, Population inversion and giant bandgap renormalization in atomically thin WS_2 layers, Nat. Photonics **9**, 466 (2015).

[13] A. Steinhoff, M. Florian, M. Rösner, G. Schönhoff, T. O. Wehling, and F. Jahnke, Exciton fission in monolayer transition metal dichalcogenide semiconductors, Nat. Commun. **8**, 1166 (2017).

[14] D. Guerci, M. Capone, and M. Fabrizio, Exciton Mott transition revisited, Phys. Rev. Mater. **3**, 054605 (2019).

[15] T. Handa, M. Holbrook, N. Olsen, L. N. Holtzman, L. Huber, H. I. Wang, M. Bonn, K. Barmak, J. C. Hone, A. N. Pasupathy, and X. Zhu, Spontaneous exciton dissociation in transition metal dichalcogenide monolayers, Sci. Adv. **10**, eadj4060 (2024).

[16] Y. Yu, A. W. Bataller, R. Younts, Y. Yu, G. Li, A. A. Puretzky, D. B. Geohegan, K. Gundogdu, and L. Cao, Room-temperature electron–hole liquid in monolayer MoS_2, ACS Nano **13**, 10351 (2019).

[17] T. B. Arp, D. Pleskot, V. Aji, and N. M. Gabor, Electron–hole liquid in a van der Waals heterostructure photocell at room temperature, Nat. Photonics **13**, 245 (2019).

[18] K. S. Rabinovich, A. N. Yaresko, R. D. Dawson, M. J. Krautloher, T. Priessnitz, Y.-L. Mathis, A. Kirilyuk, B. Keimer, and A. V. Boris, Optically driven dynamics of a Mott insulator-to-metal transition, Adv. Funct. Mater. **35**, 2416597 (2025).

[19] M. Dendzik, R. Patrick Xian, E. Perfetto, D. Sangalli, D. Kutnyakhov, S. Dong, S. Beaulieu, T. Pincelli, F. Pressacco, D. Curcio, S. Y. Agustsson, M. Heber, J. Hauer, W. Wurth, G. Brenner, Y. Acremann, P. Hofmann, M. Wolf, A. Marini, G. Stefanucci, *et al.*, Observation of an excitonic Mott transition through ultrafast core-*cum*-conduction photoemission spectroscopy, Phys. Rev. Lett. **125**, 096401 (2020).

[20] M. Karmakar, S. Mukherjee, S. K. Ray, and P. K. Datta, Electron-hole plasma formation dynamics observed through exciton-plasma interactions in transition metal dichalcogenides, Phys. Rev. B **104**, 075446 (2021).

[21] R. Huber, F. Tauser, A. Brodschelm, M. Bichler, G. Abstreiter, and A. Leitenstorfer, How many-particle interactions develop after ultrafast excitation of an electron–hole plasma, Nature (London) **414**, 286 (2001).

[22] W.-D. Schöne and W. Ekardt, Time-dependent screening of a positive charge distribution in metals: Excitons on an ultrashort time scale, Phys. Rev. B **62**, 13464 (2000).

[23] Q. Cui, F. Ceballos, N. Kumar, and H. Zhao, Transient absorption microscopy of monolayer and bulk WSe_2, ACS Nano **8**, 2970 (2014).

[24] S. Calati, Q. Li, X. Zhu, and J. Stähler, Dynamic screening of quasiparticles in WS_2 monolayers, Phys. Rev. B **107**, 115404 (2023).

[25] C. Ruppert, A. Chernikov, H. M. Hill, A. F. Rigosi, and T. F. Heinz, The role of electronic and phononic excitation in the optical response of monolayer WS_2 after ultrafast excitation, Nano Lett. **17**, 644 (2017).

[26] P. D. Cunningham, A. T. Hanbicki, K. M. McCreary, and B. T. Jonker, Photoinduced bandgap renormalization and exciton binding energy reduction in WS_2, ACS Nano **11**, 12601 (2017).

[27] E. J. Sie, A. Steinhoff, C. Gies, C. H. Lui, Q. Ma, M. Rösner, G. Schönhoff, F. Jahnke, T. O. Wehling, Y.-H. Lee, J. Kong, P. Jarillo-Herrero, and N. Gedik, Observation of exciton redshift–blueshift crossover in monolayer WS_2, Nano Lett. **17**, 4210 (2017).

[28] J. Zou, R. Zhu, J. Wang, H. Meng, Z. Wang, H. Chen, and Y.-X. Weng, Coherent phonon-mediated many-body interaction in monolayer WSe_2, J. Phys. Chem. Lett. **14**, 4657 (2023).

[29] D. Timmer, M. Gittinger, T. Quenzel, A. R. Cadore, B. L. T. Rosa, W. Li, G. Soavi, D. C. Lünemann, S. Stephan, M. Silies, *et al.*, Ultrafast coherent exciton couplings and many-body interactions in monolayer WS_2, Nano Lett. **24**, 8117 (2024).

[30] L. T. Lloyd, R. E. Wood, F. Mujid, S. Sohoni, K. L. Ji, P.-C. Ting, J. S. Higgins, J. Park, and G. S. Engel, Sub-10 fs intervalley exciton coupling in monolayer MoS_2 revealed by helicity-resolved two-dimensional electronic spectroscopy, ACS Nano **15**, 10253 (2021).

[31] M. Manca, M. M. Glazov, C. Robert, F. Cadiz, T. Taniguchi, K. Watanabe, E. Courtade, T. Amand, P. Renucci, X. Marie, G. Wang, and B. Urbaszek, Enabling valley selective exciton scattering in monolayer WSe_2 through upconversion, Nat. Commun. **8**, 14927 (2017).

[32] F. Katsch, M. Selig, and A. Knorr, Theory of coherent pump–probe spectroscopy in monolayer transition metal dichalcogenides, 2D Mater. **7**, 015021 (2020).

[33] A. Dobryakov, S. A. Kovalenko, A. Weigel, J. L. Pérez-Lustres, J. Lange, A. Müller, and N. Ernsting, Femtosecond pump/supercontinuum-probe spectroscopy: Optimized setup and signal analysis for single-shot spectral referencing, Rev. Sci. Instrum. **81**, 113106 (2010).

[34] S. A. Kovalenko, A. L. Dobryakov, J. Ruthmann, and N. P. Ernsting, Femtosecond spectroscopy of condensed phases with chirped supercontinuum probing, Phys. Rev. A **59**, 2369 (1999).

[35] S. B. Desai, S. R. Madhvapathy, M. Amani, D. Kiriya, M. Hettick, M. Tosun, Y. Zhou, M. Dubey, J. W. Ager III, D. Chrzan, and A. Javey, Gold-mediated exfoliation of ultralarge optoelectronically-perfect monolayers, Adv. Mater. **28**, 4053 (2016).

[36] F. Liu, M. E. Ziffer, K. R. Hansen, J. Wang, and X. Zhu, Direct determination of band-gap renormalization in the photoexcited monolayer MoS_2, Phys. Rev. Lett. **122**, 246803 (2019).

[37] N. Olsen, S. Yoon, M. Holbrook, M. Thinel, L. N. Holtzman, Y. Liu, V. Hsieh, Y. Li, D. D. Xu, E. Rojas-Gatjens, *et al.*, Macroscopic transition metal dichalcogenide monolayers from gold-tape exfoliation retain intrinsic properties, Nano Lett. **25**, 15198 (2025).

[38] G. Wang, A. Chernikov, M. M. Glazov, T. F. Heinz, X. Marie, T. Amand, and B. Urbaszek, *Colloquium*: Excitons in atomically thin transition metal dichalcogenides, Rev. Mod. Phys. **90**, 021001 (2018).

[39] S. Calati, Q. Li, X. Zhu, and J. Stähler, Ultrafast evolution of the complex dielectric function of monolayer WS_2 after photoexcitation, Phys. Chem. Chem. Phys. **23**, 22640 (2021).

[40] See Supplemental Material at http://link.aps.org/supplemental/10.1103/hh6p-dpf7 for additional information on the analysis of steady state absorption spectra, the V_0 parameters, extended examples of spectra and fits, especially for below and above the threshold fluence, the behavior of the ground-state bleach and the TA spectra at early pump-probe delays, and details of the abrupt changes in the peak broadening of the excitonic resonances, which includes Refs. [10,26,39,58,59].

[41] B. Tanda Bonkano, S. Palato, J. Krumland, S. Kovalenko, P. Schwendke, M. Guerrini, Q. Li, X. Zhu, C. Cocchi, and J. Stähler, Evidence for hybrid inorganic–organic transitions at the WS_2/terrylene interface, Phys. Status Solidi (A) **221**, 2300346 (2024).

[42] Y. Li and T. F. Heinz, Two-dimensional models for the optical response of thin films, 2D Mater. **5**, 025021 (2018).

[43] L. Guo, M. Wu, T. Cao, D. M. Monahan, Y.-H. Lee, S. G. Louie, and G. R. Fleming, Exchange-driven intravalley mixing of excitons in monolayer transition metal dichalcogenides, Nat. Phys. **15**, 228 (2019).

[44] J. P. Bange, P. Werner, D. Schmitt, W. Bennecke, G. Meneghini, A. Al Mutairi, M. Merboldt, K. Watanabe, T. Taniguchi, S. Steil, D. Steil, *et al.*, Ultrafast dynamics of bright and dark excitons in monolayer WSe_2 and heterobilayer WSe_2/MoS_2, 2D Mater. **10**, 035039 (2023).

[45] Y. Wang, J. Nishida, K. Nakamoto, X. Yang, Y. Sakuma, W. Zhang, T. Endo, Y. Miyata, and T. Kumagai, Ultrafast nanoimaging of spatially modulated many-body dynamics in CVD-grown monolayer WS_2, ACS Photonics **12**, 207 (2025).

[46] M. Selig, G. Berghäuser, A. Raja, P. Nagler, C. Schüller, T. F. Heinz, T. Korn, A. Chernikov, E. Malic, and A. Knorr, Excitonic linewidth and coherence lifetime in monolayer transition metal dichalcogenides, Nat. Commun. **7**, 13279 (2016).

[47] S. Sim, J. Park, J.-G. Song, C. In, Y.-S. Lee, H. Kim, and H. Choi, Exciton dynamics in atomically thin MoS_2: Interexcitonic interaction and broadening kinetics, Phys. Rev. B **88**, 075434 (2013).

[48] G. Gupta and K. Majumdar, Fundamental exciton linewidth broadening in monolayer transition metal dichalcogenides, Phys. Rev. B **99**, 085412 (2019).

[49] G. Moody, C. K. Dass, K. Hao, C.-H. Chen, L.-J. Li, A. Singh, K. Tran, G. Clark, X. Xu, G. Berghäuser, *et al.*, Intrinsic homogeneous linewidth and broadening mechanisms of excitons in monolayer transition metal dichalcogenides, Nat. Commun. **6**, 8315 (2015).

[50] J. Madéo, M. K. L. Man, C. Sahoo, M. Campbell, V. Pareek, E. L. Wong, A. Al-Mahboob, N. S. Chan, A. Karmakar, B. M. K. Mariserla, *et al.*, Directly visualizing the momentum-forbidden dark excitons and their dynamics in atomically thin semiconductors, Science **370**, 1199 (2020).

[51] R. Wallauer, R. Perea-Causin, L. Münster, S. Zajusch, S. Brem, J. Güdde, K. Tanimura, K.-Q. Lin, R. Huber, E. Malic, and U. Höfer, Momentum-resolved observation of exciton formation dynamics in monolayer WS_2, Nano Lett. **21**, 5867 (2021).

[52] H. Wang, C. Zhang, W. Chan, C. Manolatou, S. Tiwari, and F. Rana, Radiative lifetimes of excitons and trions in monolayers of the metal dichalcogenide MoS_2, Phys. Rev. B **93**, 045407 (2016).

[53] M. Palummo, M. Bernardi, and J. C. Grossman, Exciton radiative lifetimes in two-dimensional transition metal dichalcogenides, Nano Lett. **15**, 2794 (2015).

[54] D. Erkensten, S. Brem, and E. Malic, Exciton-exciton interaction in transition metal dichalcogenide monolayers and van der Waals heterostructures, Phys. Rev. B **103**, 045426 (2021).

[55] S. Mohapatra, Photoinduced ultrafast and discontinuous exciton Mott transition in monolayer WS_2, Ph.D. thesis, Humboldt University of Berlin, 2026.

[56] It should be noted that above the critical excitation density of 31×10^{12} cm^{-2}, this component seems to be missing. This likely just because it is accelerated and does not appear at 200 fs anymore (cf. Sec. S6 of the Supplemental Material [40]).

[57] A. Champagne, J. B. Haber, S. Pokawanvit, D. Y. Qiu, S. Biswas, H. A. Atwater, F. H. da Jornada, and J. B. Neaton, Quasiparticle and optical properties of carrier-doped monolayer $MoTe_2$ from first principles, Nano Lett. **23**, 4274 (2023).

[58] M. Bauer, A. Marienfeld, and M. Aeschlimann, Hot electron lifetimes in metals probed by time-resolved two-photon photoemission, Prog. Surf. Sci. **90**, 319 (2015).

[59] F. Sekiguchi, T. Mochizuki, C. Kim, H. Akiyama, L. N. Pfeiffer, K. W. West, and R. Shimano, Anomalous metal phase emergent on the verge of an exciton Mott transition, Phys. Rev. Lett. **118**, 067401 (2017).

[60] S. Mohapatra, S. Palato, J. Stähler, and L. Gierster, Fluence-dependent ultrafast broadband transient absorption data of a WS_2 monolayer on fused silica [Dataset], Zenodo, 2026, https://doi.org/10.5281/zenodo.23211020.